Realistic representation of mixed-phase clouds increases projected climate warming

Check for updates

Stefan Hofer [1,2] ✉, Lily C. Hahn [3], Jonah K. Shaw [4,5], Zachary S. McGraw [6,7], Olimpia Bruno [8], Franziska Hellmuth [2], Marianne Pietschnig [2], Idunn Aa. Mostue [9], Robert O. David [2], Tim Carlsen [2] & Trude Storelvmo [2]

Clouds are the main source of uncertainties when projecting climate change. Mixed-phase clouds that contain ice and supercooled-liquid particles are especially hard to constrain, and climate models neither agree on their phase nor their spatial extent. This is problematic, as models that underestimate contemporary supercooled-liquid in mixed-phase clouds will underestimate future warming. Furthermore, it has recently been shown that supercooled-liquid water in mixed-phase clouds is not homogeneously-mixed, neither vertically nor horizontally. However, while there have been attempts at observationally constraining mixed-phase clouds to constrain uncertainties in future warming, all studies only use the phase of the interior of mixed-phase clouds. Here we show, using novel satellite observations that distinguish between cloud-top and interior phase in mixed-phase clouds, that mixed-phase clouds are more liquid at the cloud top globally. We use these observations to constrain the cloud top phase in addition to the interior in a global climate model, leading to +1 °C more 21st century warming in NorESM2 SSP5-8.5 climate projections. We anticipate that the difference between cloud top and interior phase in mixed-phase clouds is an important new target metric for future climate model development, because similar mixed-phase clouds related biases in future warming are likely present in many climate models.

Clouds can consist of liquid, ice or a mixture of both, with distinctly different impacts on the Earth's radiation budget[1-5]. A greater fraction of liquid particles within a cloud generally leads to a higher cloud albedo and less shortwave radiation reaching the surface. Concurrently, a higher liquid water content will also increase the cloud's longwave emissivity and therefore, increase the amount of trapped longwave radiation[5,6]. Between −38 and 0 °C, liquid and ice particles can coexist, forming a mixed-phase cloud (MPC)[7,8]. Most of these MPCs are found over the Southern Ocean and the Northern Hemisphere extratropical storm track[9], but they can also exist in more extreme environments such as the Arctic and over high-latitude polar ice sheets[7,10-12]. Active satellite observations between 2006 and 2011 suggest that MPCs have a global mean cloud radiative effect of −3.4 W m^{-2}, driven by a strong cooling in the shortwave part of the spectrum[4]. While passive satellite sensors struggle to accurately detect cloud phase[13,14], active satellite

sensors such as onboard Cloudsat and the Cloud-Aerosol Lidar and Infrared Pathfinder Satellite Observation (CALIPSO) satellites provide a more accurate picture of the global distribution and climate impacts of MPCs.

MPCs are still one of the leading causes of uncertainties in projecting global climate change[15-18], despite the fact that Cloudsat and CALIPSO have been in orbit for 16 years[19], advances in ground-based observations of MPCs and more sophisticated cloud parameterizations in state-of-the-art climate models. A notable part of the uncertainty from MPCs results from the fact that even within one mixed-phase cloud system, the water and ice phases are not homogenously mixed, neither horizontally nor vertically[20,21]. Because cloud parameterizations assume homogeneously mixed ice and liquid particles, cloud parameterizations often grow too much ice at the expense of supercooled liquid droplets via a too-efficient Wegener–Bergeron–Findeisen (WBF) process[22,23]. This

[1]School of Geographical Sciences, University of Bristol, Bristol, UK. [2]Department of Geosciences, University of Oslo, Oslo, Norway. [3]Department of Atmospheric Sciences, University of Washington, Seattle, WA, USA. [4]Department of Atmospheric and Oceanic Sciences, University of Colorado, Boulder, CO, USA. [5]Cooperative Institute for Research in Environmental Science, University of Colorado, Boulder, CO, USA. [6]Department of Applied Physics and Applied Mathematics, Columbia University, New York, USA. [7]NASA Goddard Institute for Space Studies, New York, USA. [8]Institute of Meteorology and Climate Research, Karlsruhe Institute of Technology, Karlsruhe, Germany. [9]Department of Technology Systems, University of Oslo, Oslo, Norway. ✉e-mail: s.hofer@bristol.ac.uk

leads to an underestimation of liquid water at mixed-phase temperatures across most climate models[24–27]. Climate models that have too much ice in the current climate will also underestimate the temperature sensitivity to anthropogenic greenhouse gas forcing, as with warming the transition from ice to liquid produces an unrealistic increase in cloud albedo[15]. However, while there is some evidence that ice and liquid particles are not homogeneously mixed and that liquid water in MPCs often resides near the cloud top[8,28–30], little is known about the global distribution of the supercooled liquid fraction (SLF) when comparing cloud top and cloud interior. We conclude that it is imperative to treat the heterogeneity of ice and liquid patches in the mixed-phase cloud regime between −38 and 0 °C to reduce uncertainties from the MPC phase in future climate projections. However, so far this has not been done in studies that observationally constrain MPCs globally.

In this study, we use novel Cloud-Aerosol Lidar with Orthogonal Polarization (CALIOP) satellite lidar observations of the SLF in MPCs not just for the cloud interior, but for the first time also for the global cloud-top phase. We show that mixed-phase cloud tops contain more liquid on average than the cloud interior everywhere globally, a pattern that is remarkably constant year-round and over both hemispheres and has so far not been reported on a global scale. Further, we use the separate information about cloud-top and interior phases to advance our ability to constrain MPCs in a state-of-the-art Earth System Model (Norwegian Earth System Model—NorESM2)[31]. After adjusting the cloud top and interior SLF over the current climate, we find an increase in climate sensitivity of +1.0 °C for a cumulative global forcing of +100 W m^{-2} (sum of annual radiation imbalance at the top of the atmosphere, Table 1). Additionally, observationally constraining the MPC phase notably reduces the biases in top-of-the-atmosphere radiation when compared to CERES satellite observations over the current climate, which also enhances the robustness of our future climate projections. Our results—expanding the approach first tested for the Arctic in ref. [32]—provide a more sophisticated approach to constrain global mixed-phase cloud phase[5,15,33]. In our NorESM2 climate, the parameter choice for constraining the cloud top and interior phase in our simulations at the same time are notably different from only using an observational constraint on the cloud interior phase. Given that most climate models used in the Climate Model Intercomparison Project 5th and 6th phase (CMIP5, CMIP6) overestimate the ice phase in the mixed-phase temperature range[24–27], it could indicate that the climate sensitivity across the models used in the latest Intergovernmental Panel on Climate Change (IPCC) AR6 report is biased low and would increase if similar observational constraints were applied[27].

Results
A novel approach to constrain MPCs in climate models
We developed a new approach to characterize MPCs globally. With this new approach, we can distinguish between cloud top and interior SLF in MPCs globally on isotherms between −40 and 0 °C (Fig. 1a). While lidar signals are usually thought to attenuate quickly in MPCs, the CALIOP lidar penetrates far enough into opaque clouds to retrieve information about two distinct MPC layers[32,34]. Figure 1b shows that for opaque clouds, where the lidar signal is fully attenuated, the signal travels on average 1.67 ± 0.49 km (Fig. 1b) into opaque clouds globally[34]. While the lidar beam travels furthest into opaque clouds in the tropics (~2 km), it penetrates more than 1 km into opaque clouds across all latitudes (Fig. 1b, right). Observational studies show that geometric cloud depth peaks around 1 km[35,36]. Therefore, we are confident that our novel algorithm can detect cloud interiors that are at least 1 km below the sampled cloud tops in a completely different thermodynamic regime (cloud phase, temperature and height).

Widespread persistence of liquid-top mixed-phase clouds
Our novel partitioning of MPCs into cloud top and interior shows that liquid-top MPCs seem to be the rule and not the exception in the climate system globally (Fig. 1c). On the −20 °C isotherm, the difference between the 4-yr-average (2009–2013) cloud-top and interior SLF is positive

Table 1 | Global warming vs. global cumulative radiative forcing

| Forcing (W m^{-2})	Control (ΔT)	Global (ΔT)	N-ET (ΔT)	S-ET (ΔT)
25	0.7°	1.5°	0.9°	1.0°
50	1.4°	2.4°	1.7°	1.7°
75	2.0°	3.0°	2.3°	2.4°
100	2.6°	3.6°	2.9°	2.9°

everywhere, i.e. cloud tops are more liquid (Fig. 1c). Further, in the northern and southern extratropics we see the most liquid cloud tops, where MPCs contain on average between 50% and 60% more supercooled liquid in their tops than in their interiors (Fig. 1c, right). Conversely, the least difference between observed cloud-top and interior SLF occurs in the tropics, where greater convection-initiated atmospheric mixing likely hinders the formation of thermodynamically distinct cloud layers in the mixed-phase temperature range. Surprisingly, the prevalence of MPCs containing a more liquid top has not been presented globally, even though most in-situ point observations in the mid- to high-latitudes already find that liquid-top MPCs are a persistent feature locally[7,8,28–30]. Assessing the spatial distribution of cloud-top minus interior SLF in the MPC regime with our novel satellite observations—however—clearly shows that liquid-top MPCs are more widespread globally than previously thought.

Observed liquid-top MPCs also dominate the mixed-phase temperature regime when looking across all seasons, vertical levels, temperatures and areas outside of the tropics (Fig. 2a–c). Figure 2a shows that globally there is little seasonal variation in cloud interior SLFs (Fig. 2a, left curves) and cloud-top SLFs (Fig. 2a, right curves) when looking at CALIOP global satellite observations. Further, we see the most notable difference between cloud-top and cloud-interior SLF between −30 and −10 °C. Below and above this temperature regime the gap narrows slightly due to limited INP activation (T > −10 °C) and increasing heterogeneous (T < −30 °C) and homogeneous freezing of cloud droplets (T < −36 °C). Spatially, we see the most notable seasonal variability in SLF in the northern extratropics (≥30°N, Fig. 2b), while the southern extratropical (≥30°S) SLFs are very stable across all seasons (Fig. 2c). Note however, while the northern extratropical SLFs vary more throughout the year, the difference in SLF between cloud top and interior stays remarkably similar. For example, on the −20 °C isotherm the cloud-top SLF lies at 83.4% in summer (JJA) and increases to 88.5% in winter (DJF), while it also increases from 30.1% in JJA to 40.6% in the interior of the observed MPCs (Fig. 2b). We, therefore, conclude that the more liquid MPC tops compared to cloud interiors are not an artefact of spatial or temporal averaging, but rather are a remarkably robust feature of the climate system across seasons and geographical locations (Fig. 1a–c).

Constraining climate model simulations with novel mixed-phase cloud observations
Constraining MPCs globally leads to a notable cooling at the top-of-the-atmosphere (Fig. 3a, right). Overall, the unconstrained NorESM2 Control simulation with prescribed ERA-reanalysis circulation (2009–2013) produces MPCs that contain too much ice, both at the cloud top and the cloud interior compared to the CALIOP satellite observations (Fig. 3a, "Original"). After reducing the concentration of INPs, the WBF process efficiency and convective ice detrainment we get both the cloud interior (mean bias: −12.8% before, 0.3% after SLF tuning) and cloud top (mean bias: −15.3% before, 4.2% after SLF tuning) into good agreement with satellite observations (Fig. 3a left, "Constrained"). Note, that the best parameter choice strongly depends on whether we only constrain for the cloud interior (WBF factor 0.1, INP factor: 0.001, no detrainment temperature adjustment required) or for the cloud interior and cloud top at the same time (WBF factor: 0.5, INP factor: 0.001, Detrainment Temperature ramp: 5 °C; see the "Methods" section). Because we notably increase the SLF in global MPCs, we cool the top-of-the-atmosphere by −1.8 W m^{-2}, most notably in the

Fig. 1 | Novel observations of mixed-phase cloud top and interior phase. a Schematic of "previous" and "new" methods to retrieve MPC supercooled liquid fraction from CALIOP observations. COD indicates the cloud's optical depth. **b** Global opaque cloud penetration depth in km (for a detailed data description see Guzman et al., 2017)[34]. **c** CALIOP lidar observations of the difference between cloud top SLF (%) and cloud interior SLF at the −20 °C isotherm. Line graph on the right shows a cross-section of the mean SLF difference for each latitude band. Note that across all latitudes, the difference is positive, i.e., cloud tops are more liquid (darker colours indicate more liquid cloud tops).
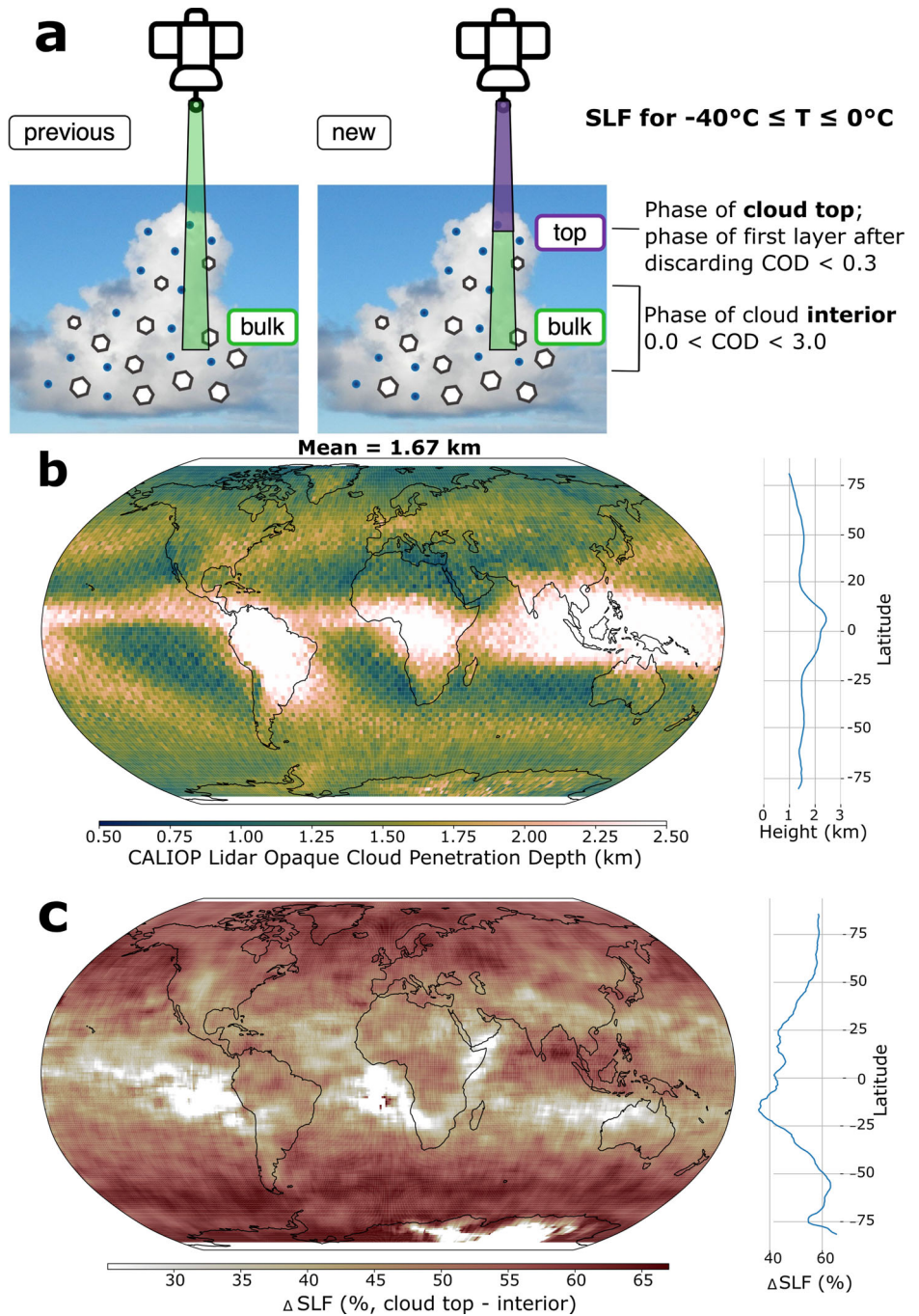
northern extratropics (−1.8 W m^{-2}) and southern extratropics (−3.6 W m^{-2}). The northern and southern extratropics are known hotspots for prevailing MPCs, and we see the largest increase in cloud liquid water content in these areas (Fig. S1A–C), alongside modest increases in cloud cover in the northern extratropics and the tropics (Fig. S1A, B). On average, we see no change in the tropical top-of-the-atmosphere net radiation balance (Fig. 3A). We conclude that increasing the SLF leads to optically thicker and brighter MPCs, which reflect more shortwave radiation back to space. This cooling by up to −8 W m^{-2} over the Southern Ocean would usually occur with warming due to a transition from the ice to the liquid phase. Therefore, in a warming climate, our observationally constrained simulations will not produce an artificially strong cooling cloud-phase feedback due to an unrealistically low base-state SLF in MPCs[37].

Constraining MPC top and interior phases in the northern and southern extratropics regionally leads to a similar local cooling as for the global constraint (Fig. 3b, c). Again, in both areas, the NorESM2 Control simulation with prescribed reanalysis circulation severely underestimates the local SLF in MPCs, both at the cloud top and in the interior (Fig. 3b, c, "Original", left). Initially, over the northern extratropics NorESM2 Control underestimates SLF by −11.5% at the cloud top and −9.9% for the cloud interior (Fig. 3b, "Original"). We find a similar underestimation of the SLF when looking at the southern extratropics (−15.9% at the cloud top and −6.8% at the cloud interior, Fig. 3c). However, in both areas we can match the observed MPC phase regionally with the same approach. By increasing the SLFs in the MPC regime more locally, we induce a top-of-the-atmosphere cooling in close alignment with our global constraint (Fig. 3b, c). Additionally, we only find limited evidence for notable radiative cooling/heating teleconnections towards the tropics or the other hemisphere when constraining MPCs only over the northern- or southern extratropics. Note, however, that in our simulation in Fig. 3, the atmospheric circulation is
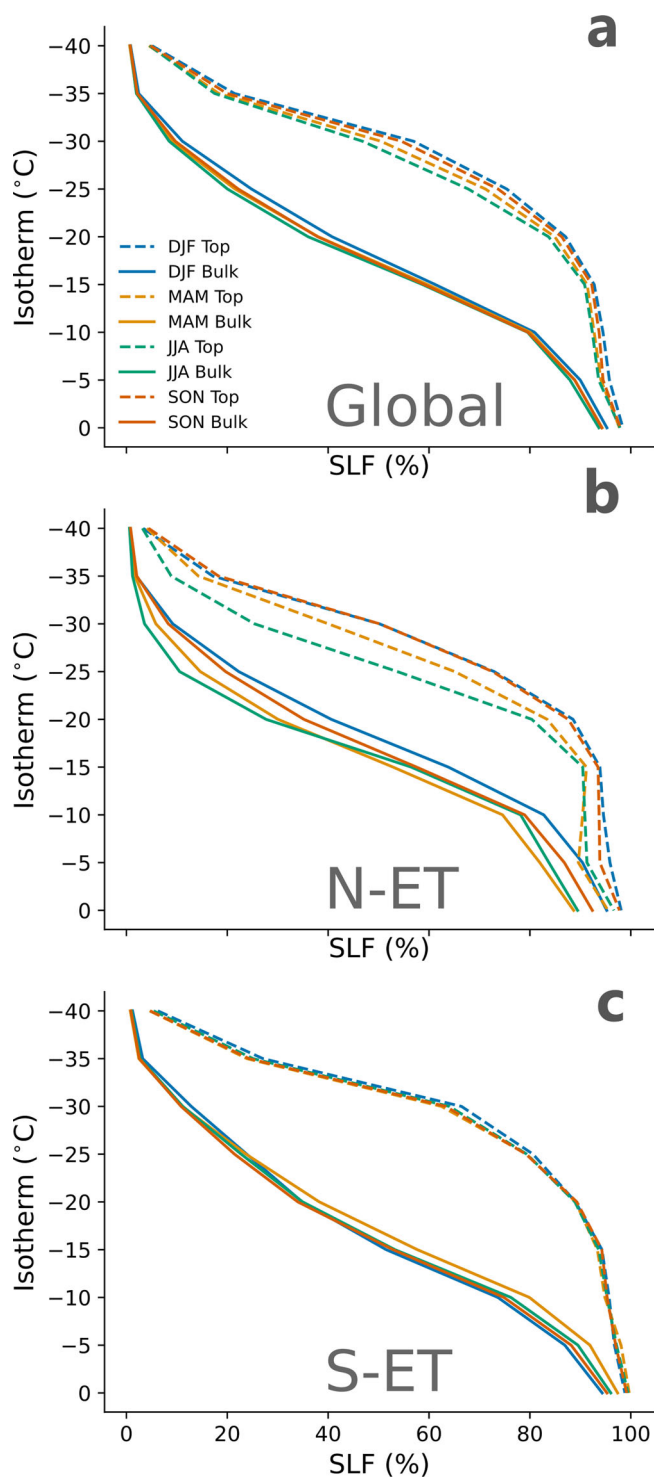
Fig. 2 | Seasonality of observed CALIOP SLF at the cloud top and interior.
a Global observed SLF in MPCs from CALIOP satellite lidar measurements. The solid lines represent the seasonal means for the cloud interior ("bulk"). The dashed lines are the SLF at the cloud-top of MPCs for different seasons. **b** Same as **a** but for the northern extratropics (north of 30°N). **c** same as **a** but for the southern extratropics (south of 30°S).

prescribed by the ERA-Interim reanalysis when we match the cloud top and cloud interior phase. Therefore, we do not allow the atmospheric circulation to react to local changes in the energy budget from increasing the liquid content of MPCs. We prescribe the synoptic-scale circulation when constraining the observed SLF in our simulations to exclude any differences in

cloud patterns and microphysics coming from changes in the atmospheric circulation patterns. This constraint is not imposed on our three fully-coupled simulations where we implement these observational constraints on global and local MPCs (3× pre-industrial control simulations, 3× historical, 3× SSP5–8.5).

Constraining mixed-phase cloud tops and interiors, additionally, also leads to a better representation of the global energy budget in NorESM2. Figure 3D shows the difference in mean bias between NorESM2 Control and our three constrained simulations—a negative value indicates a lower bias compared to the NorESM2 Control bias. It clearly shows that the absolute bias in top-of-the-atmosphere radiation between NorESM2 simulations and CERES satellite observations decreases notably when we constrain mixed-phase cloud SLFs. Globally, we find a decrease of -0.8 W m^{-2} in net radiation bias for globally constrained MPCs (NorESM2 Global) compared to the NorESM2 Control simulation (Fig. 3d, orange). The improvement in top-of-the-atmosphere net radiation is especially pronounced over the Southern Ocean (up to 8 W m^{-2}), an area of long-standing disagreements between climate models and observations[38]. Observationally constraining cloud phase locally in NorESM2 S-ET and N-ET yields very similar improvements in representing the global energy budget as in NorESM2 Global when looking at the same region (Fig. 3d).

Our results indicate that there is some evidence for cloud-phase-related teleconnections when modelling the hemispheric energy budget in the northern extratropics. Here, we focus on the comparison of the northern extratropics between the locally constrained NorESM2 N-ET simulation compared with the globally constrained NorESM2 Global. Our assumption is, because both are constrained in the northern extratropics, that any difference here would have to be a result of differences outside of the northern extratropics. Over the northern extratropics, NorESM2 Global reduces the net radiation bias compared to CERES observations more than the only locally constrained NorESM2 N-ET simulation. Conversely, we find limited evidence for notable teleconnections in the southern extratropical net radiation bias, where NorESM2 Global and NorESM2 S-ET both impact (reduce) the net top-of-the-atmosphere radiation bias equally over the southern extratropics.

Observational MPC constraints increase climate sensitivity
Our fully coupled simulations show that our global observational constraint on cloud SLF leads to the most sensitive global climate system (Fig. 4a, blue line). For example, at $+100$ W m^{-2} of cumulative top-of-the-atmosphere radiative forcing, NorESM2 Global warms by $+1.0$ °C more globally than the NorESM2 Control SSP5–8.5 submitted for CMIP6 (Fig. 4a, red line). Furthermore, we find that the two simulations where we constrain the SLF only north of 30°N (NorESM2 N-ET, orange) and south of 30°S (NorESM2 S-ET, green) both increase global climate sensitivity roughly equally compared to the NorESM2 Control simulation (red). At $+100$ W m^{-2} cumulative forcing NorESM2 N-ET and S-ET both warm by $+2.9$ °C, which is 0.3 °C more than NorESM2 Control. We conclude that observationally constraining cloud top and interior SLFs globally, notably increases the sensitivity of NorESM2 to a given radiative forcing in SSP5–8.5, which would likely also result in NorESM2 moving away from being a model with a low equilibrium climate sensitivity (ECS) towards a higher ECS[39].

Our simulations also indicate that northern extratropical (N-ET, >30°N) climate sensitivity is in large part defined by cloud-phase-related feedbacks outside of the northern extratropics (Fig. 4b). When comparing the 2015–2100 temperature increase between our globally constrained NorESM2 Global (blue) and the only locally constrained NorESM2 N-ET (orange), we see that NorESM2 Global is much more sensitive in the northern extratropics to a given cumulative radiative imbalance. However, both have observationally matched cloud phases north of 30°N. For example, at $+100$ W m^{-2} of global radiative forcing, the NorESM2 N-ET case warms by only $+4.8$ °C in the northern extratropics, whereas the globally constrained NorESM2 Global simulations warms by $+6.2$, 1.4 °C more despite the same global radiative imbalance (Table S1). Compared to the unchanged NorESM2 Control simulation, the northern extratropics
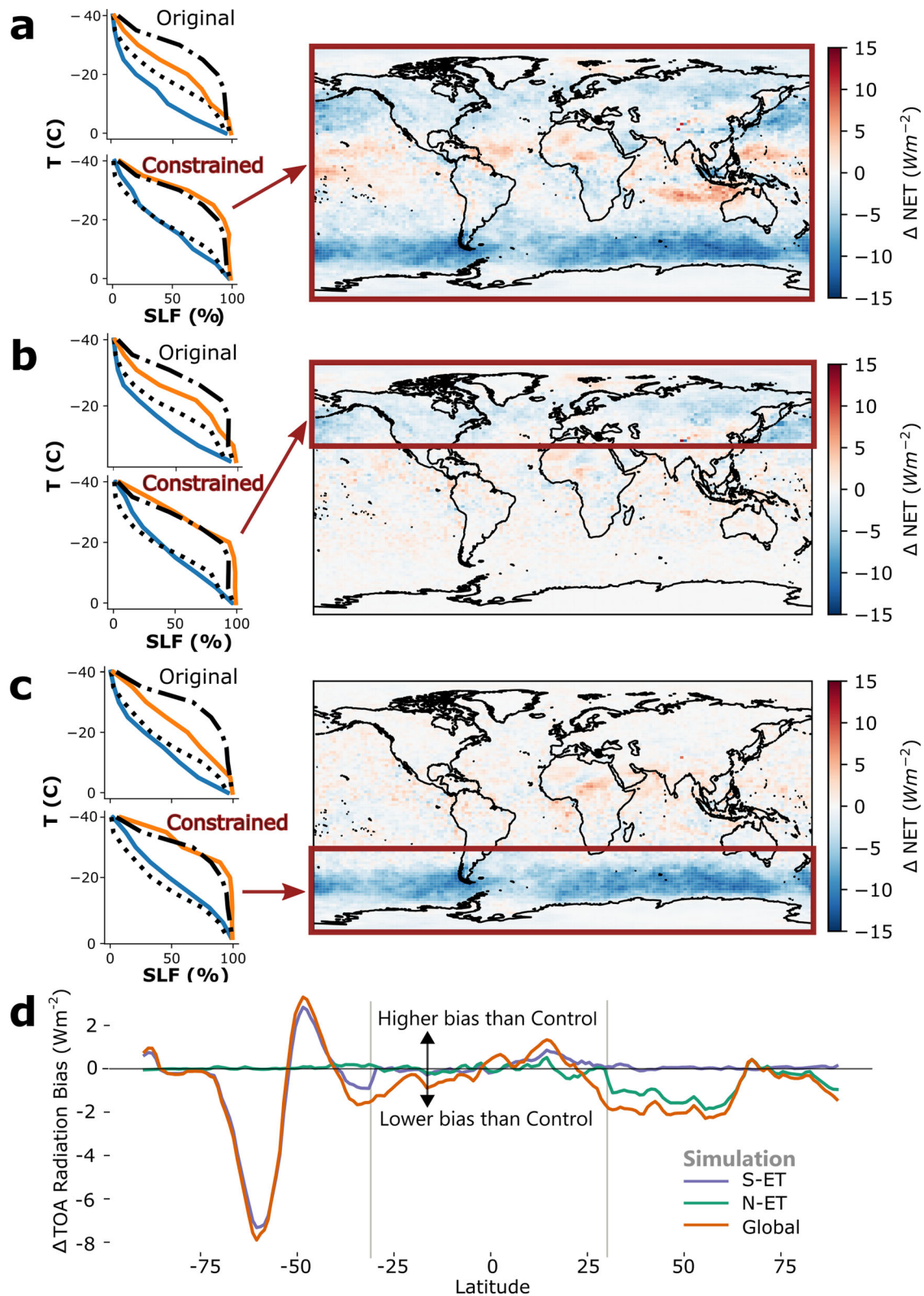
warm 1.6 times more (+6.2 °C (blue) vs. +3.8 °C (red)) at +100 W m^{-2} of global radiative forcing in the NorESM2 Global simulation, compared to only 1.25 times as much in the NorESM2 N-ET case (+4.8 °C (orange) vs.+3.8 °C (red), Table S1). Further, we also see a slight sensitivity increase in the northern extratropics when we constrain the SLFs in the southern extratropics compared to the NorESM2 Control (Fig. 4b, green, +4.4 vs. +3.8 °C) at +100 W m^{-2} global radiative imbalance (Table S1). Our results,

therefore, clearly indicate that at least half of the northern extratropical climate sensitivity changes due to observational mixed-phase SLF constraints stem from changes in the cloud feedbacks and teleconnections outside of the northern extratropics, i.e. the tropics and southern extratropics. We conclude that models that only capture the local cloud phase over the northern extratropics will still underestimate the local climate sensitivity.

Fig. 3 | Constrained SLF and its impact on top-of-the-atmosphere radiation.
a Left top "Original" NorESM2 (2009–2013) SLF (%) vs atmospheric (vertical) temperature (°C). Black lines indicate observed cloud interior (dotted) and cloud top (dash-dot) from CALIOP observations, orange and blue lines indicate NorESM2 SLF. Left bottom SLF versus temperature for the same NorESM2 setup but with observationally constrained SLF. The SLF vs. temperature figures show the SLF curves for the geographical areas indicated with the dark red rectangle on the map plot. All NorESM2 simulations used for matching CALIOP observed are with nudged ERA-Interim circulation. Map plot shows the difference in top-of-the-atmosphere (TOA) net radiation between NorESM2 Global with constrained SLF minus the unconstrained NorESM2 setup (blue indicates a cooling when SLFs are constrained). **b** Same as **a** but NorESM2 only constrained in the northern extratropics (≥30°N). **c** same as **b** but for the southern extratropics (≥30°S). **d** Absolute change in top-of-the-atmosphere radiation bias (W m⁻²) between NorESM2 Control and three NorESM2 simulations with constrained MPCs. We computed the bias for each simulation compared to CERES satellite observation first and then computed the difference between the NorESM2 Control and our three constrained simulations. A negative value indicates a lower bias in the constrained simulation than in NorESM2 Control when compared to CERES observations of TOA radiation.
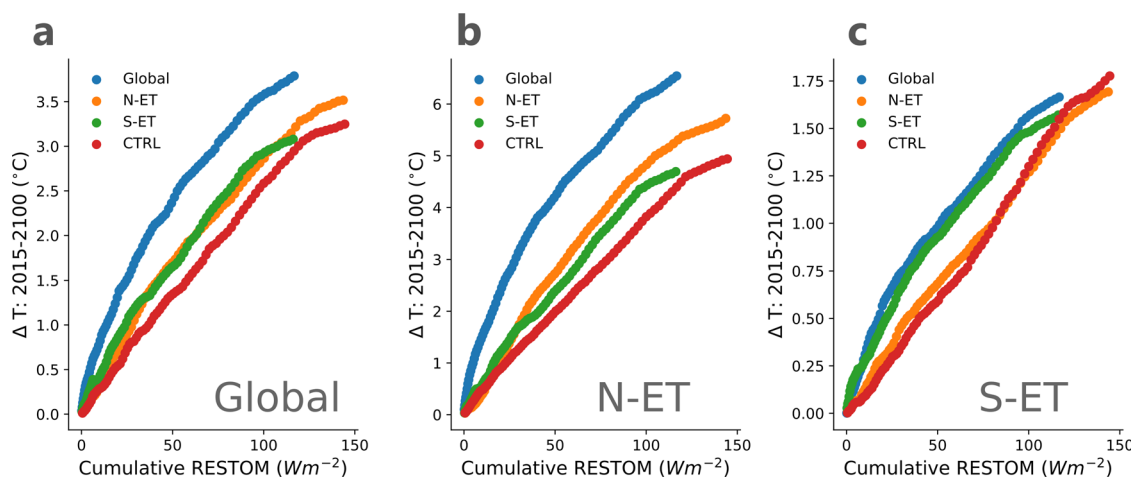

Fig. 4 | Sensitivity for a given top-of-the-atmosphere radiative imbalance between 2015 and 2100 under SSP5–8.5 forcing. a Shows the global cumulative residual top of the atmosphere radiative flux (RESTOM W m⁻²) versus the global change in temperature during the SSP5–8.5 period of 2015–2100. The further to the top left the more sensitive is a given simulation. "Control" (red) is the unchanged NorESM2 Control SSP5–8.5 simulations, "S-ET" (southern extratropics, green) refers to the simulation with constrained mixed-phase SLF south of 30°S, "N-ET" (northern extratropics, orange) refers to the simulation with constrained SLF north of 30°N and "Global" (blue) refers to the simulations where SLF is constrained globally. **b** Same as **a** but showing the northern extratropics temperature changes versus the global RESTOM. **c** same as **a** but showing the southern extratropics temperature changes versus the global RESTOM. Note the different ranges on the *y*-axis in (**a**–**c**).

The southern extratropics, conversely, seem to be only sensitive to the local cloud phase (Fig. 4c, Table S2). While the northern extratropical climate sensitivity strongly increases with cloud phase changes outside of the northern extratropics (Fig. 4b), in the southern extratropics, we see no difference between the unconstrained NorESM2 Control (red) and NorESM2 N-ET (orange). They both have a similarly low-temperature sensitivity over the southern extratropics (Fig. 4c). Conversely, NorESM2 Global and NorESM2 S-ET, both with constrained SLFs over the southern extratropics, show a notably higher sensitivity to a given forcing. At +100 W m⁻² of global radiative imbalance both warm almost exactly the same amount of +1.5 °C (S-ET 1.48 °C, Global +1.57 °C, Table S2). This strikingly similar behaviour between the globally versus locally constrained simulations over the southern extratropics is very different from the northern extratropics.

In summary, we find that (i) over the northern extratropics the climate sensitivity to a given forcing is mostly controlled by cloud-phase-induced changes elsewhere, i.e. NorESM2 Global warms more than NorESM2 N-ET (Fig. 4b), (ii) over the southern extratropics climate sensitivity is mostly controlled by local changes in cloud phase due to observational constraints (Fig. 4c), (iii) for the global climate sensitivity the southern and northern extratropics are equally important (Fig. 4a). We hypothesize that the southern extratropics react much more slowly to cloud-phase induced climate sensitivity changes elsewhere, because the upwelling bottom water across the Southern Ocean takes centuries to transport surface climate signals into the southern extratropics[40].

Contribution of cloud feedbacks to the increase in climate sensitivity

Partitioning the cloud feedback into their contributing factors highlights that differences in global climate sensitivity stem partly from a difference in global net cloud feedback (Fig. 5a[41,42]). The NorESM2 Global simulation yields global net cloud feedback in the middle of the 21st century (2041–2050 average feedbacks, regressed against the pre-industrial control climate) of +0.26 W m⁻²/K, compared to +0.16 W m⁻²/K for the unconstrained control simulation (Fig. 5a, "Total", Supplementary Fig. S2). The NorESM2 Control simulation's net cloud feedback is, therefore, 39% lower than in the NorESM2 Global simulation with constrained SLFs. The most notable contribution to the difference in global cloud feedback stems from a difference in the net cloud optical depth (Fig. 5a, "Tau") and net altitude (Fig. 5a, "Alt") feedback. The difference in the net cloud optical depth feedback mostly stems from the shortwave cloud optical depth feedback (Fig. S2, "SW-Tau"). This is a direct result of a higher global base-state SLF with globally constrained MPCs, leading to a lower increase in global cloud albedo due to less efficient ice-to-liquid phase transitions with warming.

Conversely, the most notable contribution to the global net altitude feedback difference comes from the longwave cloud altitude feedback (Fig. S2). Most of this increase in the altitude feedback comes from the changes in the tropical LW cloud feedback (Fig. S3, third panel). Here, it is well established that tropical clouds rise with warming, allowing them to trap more longwave radiation[43]. In our simulation, we affect tropical clouds by detraining more tiny liquid droplets, subsequently potentially leading to slower sedimentation rates due a larger fraction of tiny droplets compared to larger ice crystals, and therefore an apparent lifting of clouds due to being longer-lived at higher altitudes. In mid-to-high latitudes, our approach of increasing the SLFs in the mixed-phase temperature range mostly increases optically thick low-level clouds. However, this is an area where the longwave radiative kernels used to calculate the cloud feedback by Zelinka et al.[41] are not sensitive to any changes in cloud optical depth or altitude.
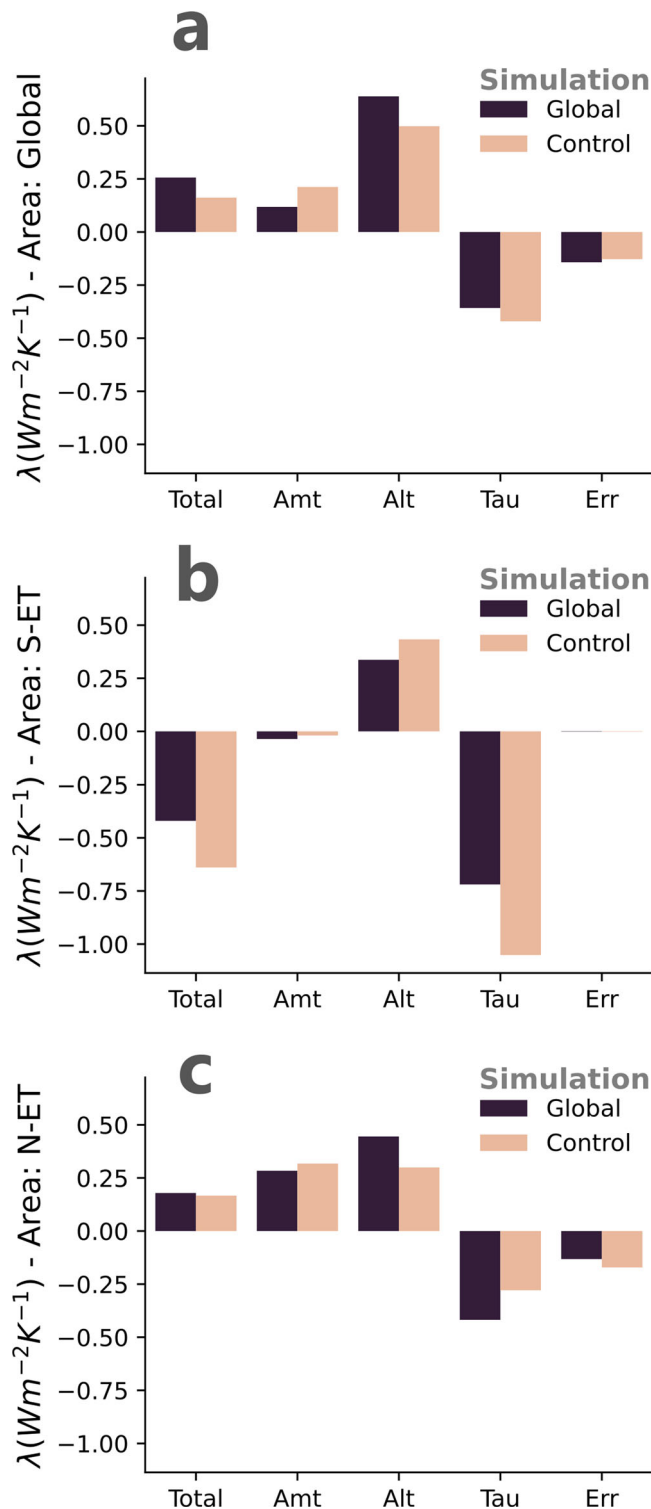
Fig. 5 | Decomposed cloud feedbacks during 2041–2050. a Net global cloud feedbacks (W m^{-2} K^{-1}, vertical axis) from the NorESM2 Global simulations (2041–2050 average) with globally constrained SLF (black), compared to the unconstrained NorESM2 Control simulation (pale pink). Shown here are the mean 2041–2050 cloud feedbacks for each simulation, regressed against the pre-industrial temperature anomalies (see the "Methods" section). **b** The horizontal axis labels describe the "Total" net cloud feedback, the net cloud amount feedback ("Amt"), the cloud altitude feedback ("Alt"), the net cloud optical depth feedback ("Tau") and the net residual term not attributed to any of the beforementioned components ("Err"). **b** Same as **a** but looking at the southern extratropics ("S-ET"). **c** Same as **a** but for the northern extratropics ("N-ET").

We see a slightly more complex behaviour when comparing the global cloud feedbacks (Fig. 5a) to those of the southern extratropics (Fig. 5b): in contrast to the global values, the total cloud feedback in the southern extratropics is negative in both simulations. The net total southern extratropical cloud feedback in NorESM2 Global is −0.42 W m^{-2}/K compared to −0.64 W m^{-2}/K in the unconstrained NorESM2 Control (Fig. 5c, "Total"). Therefore, our novel approach to constraining mixed-phase clouds globally leads to a 34% increase in the net cloud feedback over the southern extratropics. This behaviour is in line with what we expect when we tune the supercooled liquid fraction in NorESM2 to match satellite observations of MPCs over the historical period. One would expect this modification to yield a more positive/less negative net cloud feedback due to less cooling from ice-to-liquid phase transitions and less additional shortwave cooling in a warming climate. We do indeed see this behaviour when looking at the partitioning of the cloud feedbacks (Fig. 5b). Most of the difference in the total cloud feedback between NorESM2 Global and Control comes from a less negative cloud optical depth feedback with warming (Fig. 5b, "Tau"). Most of these cloud optical depth feedback differences stem further from a difference in the shortwave part of the spectrum (Fig. S2). The less negative net cloud feedback over the southern extratropics is in line with what we see when we compare the climate sensitivities in Fig. 4c.

Over the northern extratropics, we see hardly any difference in cloud feedback between the constrained NorESM2 Global simulation (0.18 W m^{-2}/K) and the NorESM2 Control simulation (0.17 W m^{-2}/K, Fig. 5c). Here, the cloud optical depth feedback is—contrary to our expectations—more negative in NorESM2 Global (−0.42 W m^{-2}/K) than in the control simulation (−0.28 W m^{-2}/K, Fig. 5c, "Tau"). This difference is mostly offset by a more positive cloud altitude feedback ("Alt"), while the cloud amount feedback is very similar. The similarity in net cloud feedback over the northern extratropics, however, further amplifies our interpretation that the change in climate sensitivity over the northern extratropics is mostly driven by changes in mixed-phased clouds outside of the northern extratropics (Fig. 4b).

Discussion

Here we observationally constrain cloud-top and interior SLF in MPCs at the same time in a global climate model. Previous studies that observationally constrained MPCs only focused on one bulk metric representative of the cloud interior phase of MPCs, thereby neglecting the vertical inhomogeneity of the water phase with distinctly more supercooled liquid concentrated in MPC tops (Fig. 1c)[33]. First, by observationally constraining cloud top and interior SLF, we show that NorESM2 can be tuned to match the global phase separation between mostly liquid cloud tops and more ice-containing MPC interiors. We find that the tuning parameters to match SLF observations for the cloud top and interior in the cloud microphysics in NorESM2 are different from matching only the cloud interior phase. Subsequently, we demonstrate that these observational constraints on cloud top and interior phase between −40 and 0 °C in NorESM2 lead to a notably more sensitive climate system (i.e. more warming for a given anthropogenic greenhouse gas forcing, Fig. 4). When constraining MPCs globally, the sensitivity for a given net top-of-the-atmosphere cumulative forcing of 50 W m^{-2} increases from warming of 1.4 to 2.4 °C, while it rises from 2.6 to 3.6 °C at 100 W m^{-2}. We present evidence that part of this increase in global climate sensitivity is driven by an increase in net cloud radiative effect (Fig. 5a) due to a less negative cloud optical depth feedback but also due to a slightly more positive cloud altitude feedback compared to NorESM2 N-ET and S-ET.

When looking at the hemispheric impacts of constrained MPCs, we find a slightly contrasting picture. While the northern extratropics' climate sensitivity increases with both local and remote cloud phase constraints, the southern extratropics only react to local changes in the cloud phase. We hypothesize that this contrasting impact of northern and southern extratropical MPCs on global climate sensitivity is due to the fact that the upwelling ocean water around Antarctica is very old and, therefore, delays the communication of climate signals from other parts of the Earth towards

the Southern Ocean[40]. However, for the global climate sensitivity, our results indicate that constraining MPCs in the northern and southern extra-tropics locally is of similar importance.

Our results emphasize that climate models that underestimate the contemporary SLF of MPC tops and interiors are very likely to project too little warming with increasing anthropogenic emissions (Fig. 4). Our Nor-ESM2 SSP5–8.5 simulations with constrained MPCs strongly indicate that observationally constraining MPC top and interior SLF leads to a better representation of key climate parameters for the contemporary climate. Most notably it decreases the bias in net top-of-the-atmosphere radiation when compared to CERES satellite observations over the current climate (Fig. 3d), creating a more physically coherent state of the climate system. When we constrain clouds globally, we reduce the global net top-of-the-atmosphere radiation bias by 0.8 W m^{-2}. This better representation of the net energy budget is especially pronounced over the Southern Ocean in NorESM2, where we reduce the local net energy flux bias by up to 8 W m^{-2}, an area of long-standing biases in the cloud phase across most climate models used in climate assessment reports[38]. Further, due to a lack of a thorough investigation of the MPC phase across all climate models used in the Intergovernmental Panel on Climate Change's latest assessment report (AR6), we believe that biases of similar magnitude are likely present in many climate models used to make policy-relevant decisions. Our results clearly show that implementing the most realistic representation of the MPC phase to date can add an additional +1 °C of 21st-century warming at a given anthropogenic forcing level. We, therefore, conclude that state-of-the-art climate models need to be validated against novel observations of MPC phase for the top and interior of MPCs to reduce the prevalent and potentially widespread biases of 21st-century warming rates.

Methods

CALIOP lidar supercooled liquid fraction observations

The observations consist of 4-year global data (from June 1, 2009 to May 31, 2013) retrieved from the CALIOP lidar v4[19,44], the active sensor onboard NASA's polar-orbiting CALIPSO satellite. We focus on cloud top and in-cloud SLF, computed globally on isotherms from −40 to 0 °C with a 5 °C increment as the ratio between the number of liquid cloud layers and the sum of ice plus liquid cloud layers (Fig. 1a). The CALIOP retrievals identify a binary ice or liquid phase for each cloud layer. The temperature data for each cloud layer is interpolated from MERRA-2 reanalysis data[45,46]. CALIOP's nominal resolution is 30 m in the vertical and 333 m in the horizontal, but here we use CALIOP Level 2 data (v.4.2)[19,44] with a horizontal resolution of 5 km before applying the 5 °C binning in the vertical. The cloud top SLF is assigned as the highest layer of the cloud once the cloud optical depth (COD) reaches 0.3[45]. This threshold (COD < 0.3) filters out any optically thin cirrus clouds and has been developed by Bruno et al.[45] to allow a like-for-like comparison with AVHRR sensors, which have notable limitations in detecting ultra-thin clouds[47]. Meanwhile, the in-cloud SLF is computed from the highest cloud layers with an accumulated optical depth of <3. To obtain the in-cloud temperatures—used for the computation of SLF on isotherms—a linear interpolation between the cloud top and bottom layers is performed taking into account the height-dependent vertical resolution of CALIOP vertical profiles.

Previously, satellite retrievals and observational climate model constraints of MPCs were purely based on the in-cloud SLF (Fig. 1a, left). Counterintuitively, MPCs often consist of a liquid layer at the cloud top, where temperatures are colder than in the interior[7,8,28–30,38]. The additional observational constraint on liquid cloud layers in global MPC tops notably changes our parameter choice to match the cloud-top phase in NorESM2. Therefore, the observed cloud-top phase is a powerful additional parameter to narrow down uncertainties in cloud-climate feedback and the general contribution of MPCs to climate sensitivity.

Norwegian Earth System Model 2

In this study, we use the second version of the Norwegian Earth System Model (NorESM2)[31], which is a slightly modified version of the Community Earth System Model (CESM2)[48]. The biggest difference between the two models is that NorESM2 contains a different ocean and ocean bio-geochemistry model. However, the most relevant difference between Nor-ESM2 and CESM2 in relation to our study design is the different treatment of aerosols and their interaction with clouds and atmospheric radiation in NorESM2[31,49,50]. The atmospheric component of NorESM2 is based on the Community Atmosphere Model version 6 (CAM6), which contains a two-moment cloud microphysics scheme with prognostic mixing ratios for different water species in addition to prognostic cloud particle number concentrations[16]. We run our simulations with NorESM2-MM, with a 1.25° × 0.9375° horizontal land and atmosphere horizontal grid spacing. The atmosphere contains 32 vertical hybrid pressure levels with a rigid lid at 3.6 hPa. For the fully coupled simulations, we run the ocean model in NorESM2 (BLOM) on a tripolar grid with 53 vertical layers and an approximate horizontal resolution of 1° zonally and 0.25° meridionally (at the Equator). Throughout our study we use latitudinally weighted monthly mean output from NorESM2.

Implementation of observational constraints in NorESM2

Based on our new method to extract robust information about the MPC top phase in addition to the cloud interior phase, we constrain the SLF in our global climate model NorESM2[31]. We observationally constrain the model's SLF between −40 and 0 °C within three fully coupled NorESM2 simulations. We constrain the SLF (1) globally, (2) for the northern extratropics north of 30°N and (3) for the southern extratropics south of 30°S for the period 2009–2013 when we have concurring CALIOP satellite observations. We have compared global SLFs for a one-year period with the average over four years and found no notable difference. Additionally, the seasonal and, therefore, intra-annual variability of the global SLF (Fig. 2a) is also very low. Therefore, the data strongly suggests that interannual variability in global mean SLF is minimal. Initially, we use atmosphere-only NorESM2 simulations with prescribed ERA-Interim reanalysis atmospheric circulation to exclude any confounding influence from circulation changes between the simulations when matching the observed SLFs (Fig. 3a–c, left). Hereby, we change the efficiency of the WBF process, the concentration of aerosols acting as ice nucleating particles for heterogeneous freezing of liquid droplets in the mixed-phase temperature range and the temperature at which detrainment from convection switches from the ice phase to liquid (see the "Methods" section and ref. 32 for a detailed description). After we minimize the mean bias between observations and atmosphere-only simulations with prescribed reanalysis circulation, we then implement the same changes to the cloud microphysics in three fully coupled NorESM2 pre-industrial control, historical and SSP5–8.5 simulations. We use the novel information about cloud-top and interior SLF to constrain MPCs via adjustments in the cloud microphysics in NorESM2[51–53], which uses a variation of CAM6 also used in CESM2[48]. Here, we focus our efforts on three distinct parts of the microphysics of the model, namely (1) the efficiency of the WBF process, (2) the amount of ice-nucleating particles (INPs) forming ice through heterogeneous nucleation and (3) the detrainment of ice particles from convection. Additionally, we first develop microphysical adjustment parameters to match the global (82°N to 82°S) observed distribution of the SLF from CALIOP between −40 and 0 °C, before also adjusting MPC phase only for the northern extra-tropics north of 30°N and for the southern extratropics south of 30°S. More local adjustments allow us to compare whether the tuning to local observations is notably different from adjusting the cloud phase globally and whether we see strong teleconnections between locally constrained cloud phase and global climate feedback.

A common thread across all three simulations is that we have to reduce the efficiency of the WBF process, the number of INPs heterogeneously nucleating ice and the amount of ice detrained from convection to account for the overestimation of ice at mixed-phase temperatures in NorESM2 (Table 2).

We reduce the efficiency at which ice crystals grow at the expense of liquid droplets by 50% (WBF factor: 0.5) across all three simulations

Table 2 | Parameter choices to observationally constrain mixed-phase clouds in NorESM2

Modification	Control	Global	N-ET	S-ET
INP factor	1	0.001	0.001	0.001
WBF factor	1	0.5	0.5	0.5
T_{Ramp}	30°	5°	15°	10°
$T_{Liquid\_Detrainment}$	−5°	−30°	−20°	−25°
$T_{Ice\_Detrainment}$	−35°	−35°	−35°	−35°

compared to the control simulation of NorESM2 used for CMIP6 (Table 2). Generally, our aim is to increase the SLF in MPCs and match CALIOP SLF observations as accurately as possible. We see the main reason behind having to strongly reduce the WBF process efficiency in NorESM2 is the fact that climate models assume a homogeneous mixture of ice and liquid particles within one grid box. Therefore, the efficiency at which ice crystals grow and deplete the amount of liquid in the mixed-phase temperature range is likely too efficient. Previous studies have clearly shown that ice and liquid droplets are more commonly found in separate pockets, minimizing the contact area between parts of MPCs where the WBF could occur[20–22,28,54]. Zhang et al. (2019)[20], for example, found that the volumes where ice and liquid particles are homogeneously mixed made up only roughly 15% of all clouds in the mixed-phase temperature range during the HIAPER Pole-to-Pole Observations (HIPPO) campaign. Additionally, the environmental vapour pressure depends on the vertical velocity, where even relatively weak updrafts caused by regular convection, atmospheric waves or turbulence can be enough to create an environment where ice and liquid particles grow simultaneously, rendering the WBF process less important. This adds to uncertainties in the MPC phase from subgrid parameterizations in global climate models[22].

However, most of these observational studies on phase heterogeneity use the horizontal distribution of ice and liquid pockets to make assumptions about the limited contact area between the ice and liquid phase. Our study, however, adds novel information about the vertical inhomogeneity by showing that liquid water is more likely to be observed in cloud tops globally, while MPC interiors are statistically more likely to be made up of ice? (Figs. 1 and 2)[7].

Furthermore, we reduce the amount of INPs available across all simulations by a factor of 10^3 (INP factor: 0.001). Observational studies show that INPs are important for controlling cloud phase[55–57] and that climate models overestimate the amount of activated INPs in regions with the most frequent MPCs. This is especially pronounced over the Southern Ocean and the Arctic, where model INP concentration can be orders of magnitude too high[58–60]. Regions with the most frequent MPCs often have very pristine oceanic air masses with very few INPs[61,62]. We conclude that we have to reduce the number of active INPs in NorESM2 by orders of magnitude, but the exact value also depends on the values chosen for the other fit parameters as also found in perturbed parameter ensemble experiments in CAM6[63].

Lastly, in addition to limiting the WBF process efficiency and INP concentrations, we also change the linear relationship that controls the phase of cloud particles being detrained from convective updrafts in NorESM2. Generally, in NorESM2 and most other GCMs, convective cores have no effect on the radiative transfer in the model. However, the convection scheme calculates the convective mass fluxes, alongside the level at which cloud condensate is detrained and subsequently enters stratiform clouds. In our study, we only change the microphysics of stratiform clouds. As soon as the cloud condensate is detrained from convection and enters a stratiform cloud, it becomes "visible" to radiation. Additionally, convective mass detrainment is a source term for ice and liquid in the stratiform cloud scheme of NorESM2. What proportion of the detrained convective cloud condensate enters the stratiform cloud scheme in the form of liquid vs. ice is usually a function of temperature.

This is the function we adjust in this study, to allow more liquid to enter the stratiform clouds from convection.

In the unchanged NorESM2 Control, the relationship states that below −35 °C all particles detrained from convection consist of ice ($T_{Ice\_Detrainment}$, Table 2), while all particles detrained above −5 °C ($T_{Liquid\_Detrainment}$, Table 2) are liquid droplets. Between $T_{Ice\_Detrainment}$ and $T_{Liquid\_Detrainment}$ there is a linear temperature ramp that defines the fraction of ice to liquid particles as

$$r = \frac{T_{Liquid\_Detrainment} - T}{T_{Ramp}}, \tag{1}$$

where T is the temperature of the convective updraft for temperatures between $T_{Liquid\_Detrainment}$ and $T_{Ice\_Detrainment}$ and

$$T_{Ramp} = T_{Liquid\_Detrainment} - T_{Ice\_Detrainment}. \tag{2}$$

In our simulations we keep the temperature below which all of the detrained particles are considered ice crystals constant, but notably, lower the temperature above which all particles are considered liquid droplets in NorESM2 from −5 °C in NorESM2 Control to between −20 and −30 °C (see Table 2). Thereby, we increase liquid detrainment from convective cores, leading to an overall increase of SLF in MPCs.

Description of simulations
Overall, we run three different fully coupled sets of simulations (pre-industrial, historical and SSP5–8.5) with constrained MPC top and interior phases. We use 4-year-long atmosphere-only simulations to match CALIOP MPC phase observations (top and interior) to NorESM2 cloud phase between 2009 and 2013 as done for the Arctic in ref. 31.

NorESM2 control. Version of NorESM2-MM (~1° resolution) used for the CMIP6 model intercomparison project. We use the pre-industrial, historical and extreme high-emission scenario SSP5–8.5 simulations in this study as a baseline for our runs with observationally constrained MPCs.

NorESM2 global. Same general setup as above, but we use CALIOP lidar observations of global MPC top and interior phase to constrain the cloud phase between 82°S and 82°N. First, we nudge the ERA-Interim circulation over 2009–2013 to create the best fit between observed SLF in MPCs from the CALIOP lidar and NorESM2[64], which we compare to a nudged NorESM2 Control simulation for the same period. Afterwards, we produce fully coupled simulations for pre-industrial, historical and SSP5-8.5 (until 2100) using the same cloud phase tuning parameters.

NorESM2 N-ET. Same as NorESM2 Global, but we use CALIOP lidar observations of global MPC top and interior phase to constrain cloud phase only in the northern extratropics between 30°N and 82°N.

NorESM2 S-ET. Same as NorESM2 Global, but we use CALIOP lidar observations of global MPC top and interior phase to constrain cloud phase only in the southern extratropics between 82°S and 30°S.

Calculation of cloud feedback in NorESM2 simulations
To disentangle the contributing factors to the difference in global warming and climate sensitivity coming from cloud-climate feedbacks between NorESM2 simulations with observationally constrained MPCs and unconstrained cloud phase, we use the radiative kernel technique described in refs. 40,41. Hereby, we gain information about the net total, amount, altitude and optical depth feedback, in addition to a residual term that cannot be attributed to any of these categories. These are further divided into their shortwave, longwave and net contributions.

To compute and partition the cloud feedback, we turn on the Cloud Feedback Model Intercomparison Project (CFMIP) Observational

Simulator Package v.2 (COSP2)[65] in NorESM2 for a 10-year period, every 50 years. Therefore, we can only compute cloud feedback in the SSP5–8.5 period during 2041–2050 and 2091–2100. Generally, we regress the changes in cloud radiative fluxes from cloud kernels onto the global temperature anomaly between the pre-industrial control climates of our simulations and the corresponding time period where we have COSP output for cloud feedback calculations, for example, 2041–2050. In theory, we can compute the cloud feedback compared to the pre-industrial control climate in this way for 1941–1950 (historical), 1991–2000 (historical), 2041–2050 (SSP58.5) and 2091–2100 (SSP58.5). However, we mostly focus on the period 2041-2050, as this is the period where the climate sensitivities diverge the most in our simulations. Cloud feedback over the historical period is not meaningful as the temperature changes are close to 0 compared to the pre-industrial control climate, and therefore regressing (i.e., dividing) by the temperature anomalies does not yield meaningful results. We restrict the use of the additional outputs from COSP2 because it adds around 20% of computational costs to an already computationally expensive fully coupled and high-resolution NorESM2 setup. Despite using a non-standard transient climate setup to compute cloud feedback in SSP5-8.5, our cloud feedback values are similar in magnitude to those found by Zelinka et al.[17], Gjermundsen et al.[66] and Zelinka et al. [67].

New climate sensitivity metric for transient climate simulations

Throughout this manuscript, we are interested in how and why climate sensitivity changes when we observationally constrained mixed-phase clouds. We have focused on a more "realistic" set of simulations that explore transient climate change through the end of the 21st century. However, standard assessments of equilibrium climate sensitivity use highly idealized simulations in which atmospheric CO_2 concentrations are instantaneously quadrupled ($4 \times CO_2$). This quadrupling approach cannot explore the transient influence of cloud changes on climate in the 21st century. Furthermore, short $4 \times CO_2$ experiments have been shown to underestimate climate sensitivity in the presence of large non-linearities in climate feedbacks[68]. To evaluate the transient climate response to constraining mixed-phase clouds, we introduce a new climate sensitivity metric suitable to simulations using SSP and RCP forcing scenarios.

$$\text{Cumulative RESTOM} = \sum_{i=2015}^{2100} \text{RESTOM}_i = \sum_{i=2015}^{2100} (\text{SWN} + \text{LWN})_i$$

(3)

We compare globally and regionally averaged surface temperatures with the global cumulative residual top of the atmosphere radiative flux (Cumulative RESTOM W m^{-2}, Eq. (3)). RESTOM captures the total energy accumulated in the earth system—the sum of net shortwave (SWN) and net longwave (LWN) radiation (Eq. (3))—due to the integrated effect of instantaneous forcings, climate feedbacks, and fast adjustments. Comparing surface temperatures and RESTOM captures both how quickly the earth system accumulates energy as well as the associated surface temperature response. Models that warm more for a given RESTOM are more responsive to the accumulated imbalance, or "energy-sensitive". By additionally studying how the relationship between surface temperature and RESTOM evolves in time (e.g. with prescribed CO_2 increases), we are able to explore the transient climate response. The times and greenhouse gas levels at which a given RESTOM is reached quantify the varying radiative forcings across model simulations. For example, a more energy-sensitive model may not warm as quickly as a less energy-sensitive model if energy accumulates more slowly in the earth system. Ultimately, we wish to explain model-to-model differences through the different rates at which models accumulate energy (the integrated radiative forcing via RESTOM) and their surface temperature sensitivity to that accumulated energy (energy-sensitivity).

Data availability

All data in this study is available to the public without restrictions (where the data has been produced by us). Most of the data in this study can be accessed at https://zenodo.org/record/8302312 (https://doi.org/10.5281/zenodo.

8302312). Fig. 1b—the underlying data can be downloaded from https://climserv.ipsl.polytechnique.fr/cfmip-obs/Calipso_goccp.html#Map_OPAQand is discussed in ref. 34. Fig. 1c—the data for the cloud top and interior SLF can be accessed via[45] under https://zenodo.org/record/8289058[69]. Fig. 2—the data for the cloud top and interior SLF can be accessed via[45] under https://zenodo.org/record/8289058. Fig. 3—the nudged NorESM2 simulations can be accessed via https://doi.org/10.5281/zenodo.8302312[69]. Fig. 4—the data underlying the sensitivity analysis can be accessed via https://doi.org/10.5281/zenodo.8302312. Fig. 5—the calculated cloud feedbacks can be accessed via https://doi.org/10.5281/zenodo.8302312.

Code availability

All code used to analyse the data presented in this study is available via https://doi.org/10.5281/zenodo.8305941.

References

1. Ramanathan, V. et al. Cloud-radiative forcing and climate: results from the earth radiation budget experiment. *Science* **243**, 57–63 (1989).
2. Shupe, M. D. & Intrieri, J. M. Cloud radiative forcing of the arctic surface: the influence of cloud properties, surface albedo, and solar zenith angle. *J. Clim.* **17**, 616–628 (2004).
3. Bennartz, R. et al. July 2012 Greenland melt extent enhanced by low-level liquid clouds. *Nature* **496**, 83–86 (2013).
4. Matus, A. V. & L'Ecuyer, T. S. The role of cloud phase in earth's radiation budget. *J. Geophys. Res.* **122**, 2559–2578 (2017).
5. Cesana, G. & Storelvmo, T. Improving climate projections by understanding how cloud phase affects radiation. *J. Geophys. Res.* **122**, 4594–4599 (2017).
6. Oreopoulos, L., Cho, N., Lee, D. & Kato, S. Radiative effects of global modis cloud regimes. *J. Geophys. Res.* **121**, 2299–2317 (2016).
7. Morrison, H. et al. Resilience of persistent Arctic mixed-phase clouds. *Nat. Geosci.* **5**, 11–17 (2012).
8. Shupe, M. D. et al. A focus on mixed-phase clouds. *Bull. Am. Meteorol. Soc.* **89**, 1549–1562 (2008).
9. Zhang, D., Wang, Z. & Liu, D. A global view of midlevel liquid-layer topped stratiform cloud distribution and phase partition from calipso and cloudsat measurements. *J. Geophys. Res. Atmos.* **115**, D00H13 (2010).
10. Lawson, R. P. & Gettelman, A. Impact of antarctic mixed-phase clouds on climate. *Proc. Natl Acad. Sci. USA* **111**, 18156–18161 (2014).
11. Lenaerts, J. T. M., Gettelman, A., Tricht, K. V., Kampenhout, L. & Miller, N. B. Impact of cloud physics on the Greenland ice sheet near-surface climate: a study with the community atmosphere model. *J. Geophys. Res.* **125**, https://onlinelibrary.wiley.com/doi/abs/10.1029/2019JD031470 (2020).
12. Klein, S. A. et al. Intercomparison of model simulations of mixed-phase clouds observed during the arm mixed-phase arctic cloud experiment. i: single-layer cloud. *Q. J. R. Meteorol. Soc.* **135**, 979–1002 (2009).
13. King, M. D., Platnick, S., Menzel, W. P., Ackerman, S. A. & Hubanks, P. A. Spatial and temporal distribution of clouds observed by modis onboard the terra and aqua satellites. *IEEE Trans. Geosci. Remote Sens.* **51**, 3826–3852 (2013).
14. Karlsson, K. G. et al. Clara-a2: The second edition of the cm saf cloud and radiation data record from 34 years of global AVHRR data. *Atmos. Chem. Phys.* (2017).
15. Tan, I., Storelvmo, T. & Zelinka, M. D. Observational constraints on mixed-phase clouds imply higher climate sensitivity. *Science* **352**, 224–227 (2016).
16. Gettelman, A. et al. High climate sensitivity in the community earth system model version 2 (cesm2). *Geophys. Res. Lett.* **46**, 8329–8337 (2019).

17. Zelinka, M. D. et al. Causes of higher climate sensitivity in cmip6 models. *Geophys. Res. Lett.* **47**, 1–12 (2020).

18. Myers, T. A. et al. Observational constraints on low cloud feedback reduce uncertainty of climate sensitivity. *Nat. Clim. Change* **11**, 501–507 (2021).

19. Winker, D. M. et al. Overview of the calipso mission and caliop data processing algorithms. *J. Atmos. Ocean. Technol.* **26**, 2310–2323 (2009).

20. Zhang, M. et al. Impacts of representing heterogeneous distribution of cloud liquid and ice on phase partitioning of arctic mixed-phase clouds with ncar cam5. *J. Geophys. Res.* **124**, 13071–13090 (2019).

21. Sokol, A. B. & Storelvmo, T. The spatial heterogeneity of cloud phase observed by satellite. *J. Geophys. Res. Atmos.* **129**, e2023JD039751 (2022).

22. Korolev, A. Limitations of the Wegener–Bergeron–Findeisen mechanism in the evolution of mixed-phase clouds. *J. Atmos. Sci.* **64**, 3372–3375 (2007).

23. Storelvmo, T. & Tan, I. The Wegener–Bergeron–Findeisen process — its discovery and vital importance for weather and climate. *Meteorol. Z.* **24**, 455–461 (2015).

24. Komurcu, M. et al. Intercomparison of the cloud water phase among global climate models. *J. Geophys. Res.* **119**, 3372–3400 (2014).

25. Cesana, G., Waliser, D. E., Jiang, X. & Li, J. F. Multimodel evaluation of cloud phase transition using satellite and reanalysis data. *J. Geophys. Res.* **120**, 7871–7892 (2015).

26. McIlhattan, E. A., L'Ecuyer, T. S. & Miller, N. B. Observational evidence linking arctic supercooled liquid cloud biases in CESM to snowfall processes. *J. Clim.* **30**, 4477–4495 (2017).

27. Cesana, G., Khadir, T., Chepfer, H. & Chiriaco, M. Southern ocean solar reflection biases in cmip6 models linked to cloud phase and vertical structure representations. *Geophys. Res. Lett.* **49**, https://onlinelibrary.wiley.com/doi/10.1029/2022GL099777 (2022).

28. Korolev, A. et al. Mixed-phase clouds: progress and challenges. *Meteorol. Monogr.* **58**, 5.1–5.50 (2017).

29. McFarquhar, G. M. et al. Indirect and semi-direct aerosol campaign: The impact of arctic aerosols on clouds. *Bull. Am. Meteorol. Soc.* **92**, 183 – 201 (2011).

30. Shupe, M. D. et al. Clouds at Arctic atmospheric observatories. Part I: Occurrence and macrophysical properties. *J. Appl. Meteor. Climatol.* **50**, 626–644 (2011).

31. Seland, O. et al. Overview of the norwegian earth system model (noresm2) and key climate response of cmip6 deck, historical, and scenario simulations. *Geosci. Model Dev.* **13**, (2020).

32. Shaw, J., McGraw, Z., Bruno, O., Storelvmo, T. & Hofer, S. Using satellite observations to evaluate model microphysical representation of arctic mixed-phase clouds. *Geophys. Res. Lett.* **49**, https://onlinelibrary.wiley.com/doi/10.1029/2021GL096191 (2022).

33. Tan, I. & Storelvmo, T. Evidence of strong contributions from mixed-phase clouds to arctic climate change. *Geophys. Res. Lett.* **46**, 2894–2902 (2019).

34. Guzman, R. et al. Direct atmosphere opacity observations from Calipso provide new constraints on cloud–radiation interactions. *J. Geophys. Res.* **122**, 1066–1085 (2017).

35. Sun-Mack, S. et al. Integrated cloud-aerosol-radiation product using ceres, modis, calipso, and cloudsat data. In *Remote Sensing of Clouds and the Atmosphere XII*, Vol. 6745, 277–287 (SPIE, 2007).

36. Lu, X. et al. Satellite retrieval of cloud base height and geometric thickness of low-level cloud based on calipso. *Atmos. Chem. Phys.* **21**, 11979–12003 (2021).

37. Bjordal, J., Storelvmo, T., Alterskjær, K. & Carlsen, T. Equilibrium climate sensitivity above 5 °C plausible due to state-dependent cloud feedback. *Nat. Geosci.* **13**, 718–721 (2020).

38. Bodas-Salcedo, A. et al. Large contribution of supercooled liquid clouds to the solar radiation budget of the southern ocean. *J. Clim.* **29**, 4213 – 4228 (2016).

39. Forster, P. et al. The earth's energy budget, climate feedbacks, and climate sensitivity. In *Climate Change 2021: The Physical Science Basis. Contribution of Working Group I to the Sixth Assessment Report of the Intergovernmental Panel on Climate Change*, *book section 7* (eds Masson-Delmotte, V. et al.) (Cambridge University Press, Cambridge, UK and New York, NY, USA, 2021).

40. Armour, K. C., Marshall, J., Scott, J. R., Donohoe, A. & Newsom, E. R. Southern Ocean warming delayed by circumpolar upwelling and equatorward transport. *Nat. Geosci.* **9**, 549–554 (2016).

41. Zelinka, M. D., Klein, S. A. & Hartmann, D. L. Computing and partitioning cloud feedbacks using cloud property histograms. Part I: cloud radiative kernels. *J. Clim.* **25**, 3715–3735 (2012).

42. Zelinka, M. D., Klein, S. A. & Hartmann, D. L. Computing and partitioning cloud feedbacks using cloud property histograms. Part I: Cloud radiative kernels. *J. Clim.* **25**, (2012).

43. Ceppi, P., Brient, F., Zelinka, M. D. & Hartmann, D. L. Cloud feedback mechanisms and their representation in global climate models. *WIREs Clim. Change* **8**, e465 (2017).

44. Liu, Z. et al. Discriminating between clouds and aerosols in the caliop version 4.1 data products. *Atmos. Meas. Tech.* **12**, 703–734 (2019).

45. Bruno, O., Hoose, C., Storelvmo, T., Coopman, Q. & Stengel, M. Exploring the cloud top phase partitioning in different cloud types using active and passive satellite sensors. *Geophys. Res. Lett.* **48**, (2021).

46. Gelaro, R. et al. The modern-era retrospective analysis for research and applications, version 2 (merra-2). *J. Clim.* **30**, 5419 – 5454 (2017).

47. Stengel, M. et al. The clouds climate change initiative: assessment of state-of-the-art cloud property retrieval schemes applied to AVHRR heritage measurements. *Remote Sens. Environ.* **162**, 363–379 (2015).

48. Danabasoglu, G. et al. The community earth system model version 2 (CESM2). *J. Adv. Model. Earth Syst.* **12**, 35 (2020).

49. Kirkevåg, A. et al. Aerosol-climate interactions in the Norwegian earth system model— NorESM1-M. *Geosci. Model Dev.* **6**, 207–244 (2013).

50. Kirkevåg, A. et al. A production-tagged aerosol module for earth system models, OsloAero5.3-extensions and updates for CAM5.3-Oslo. *Geosci. Model Dev.* **11**, 3945–3982 (2018).

51. Gettelman, A. & Morrison, H. Advanced two-moment bulk microphysics for global models. Part I: Off-line tests and comparison with other schemes. *J. Clim.* **28**, 1268–1287 (2015).

52. Hoose, C., Lohmann, U., Bennartz, R., Croft, B. & Lesins, G. Global simulations of aerosol processing in clouds. *Atmos. Chem. Phys.* **8**, 6939–6963 (2008).

53. Hoose, C., Kristjánsson, J. E. & Burrows, S. M. How important is biological ice nucleation in clouds on a global scale? *Environ. Res. Lett.* **5**, 024009 (2010).

54. Korolev, A. & Milbrandt, J. How are mixed-phase clouds mixed? *Geophys. Res. Lett.* **49**, e2022GL099578 (2022).

55. Carlsen, T. & David, R. O. Spaceborne evidence that ice-nucleating particles influence high-latitude cloud phase. *Geophys. Res. Lett.* **49**, e2022GL098041 (2022).

56. Creamean, J. M. et al. Annual cycle observations of aerosols capable of ice formation in central arctic clouds. *Nat. Commun.* **13**, 3537 (2022).

57. Sze, K. C. H. et al. Ice-nucleating particles in northern Greenland: annual cycles, biological contribution and parameterizations. *Atmos. Chem. Phys.* **23**, 4741–4761 (2023).

58. Vergara-Temprado, J. et al. Strong control of southern ocean cloud reflectivity by ice-nucleating particles. *Proc. Natl Acad. Sci.* **115**, 2687–2692 (2018).

59. Vignon, E. et al. Challenging and improving the simulation of mid-level mixed-phase clouds over the high-latitude southern ocean. *J. Geophys. Res.* **126**, https://onlinelibrary.wiley.com/doi/10.1029/2020JD033490 (2021).

60. Li, G., Wieder, J., Pasquier, J. T., Henneberger, J. & Kanji, Z. A. Predicting atmospheric background number concentration of ice-

nucleating particles in the Arctic. *Atmos. Chem. Phys.* **22**, 14441–14454 (2022).
61. McCluskey, C. S. et al. Observations of ice nucleating particles over Southern Ocean waters. *Geophys. Res. Lett.* **45**, 11,989–11,997 (2018).
62. McCluskey, C. S. et al. Marine and terrestrial organic ice-nucleating particles in pristine marine to continentally influenced northeast Atlantic air masses. *J. Geophys. Res.* **123**, (2018).
63. Eidhammer, T., Gettelman, A. & Thayer-Calder, K. Cesm2.2-cam6 perturbed parameter ensemble (ppe) (2023) (accessed 15 May 2023); Data retrieved from https://doi.org/10.26024/bzne-yf09.
64. Dee, D. P. et al. The era-interim reanalysis: configuration and performance of the data assimilation system. *Q. J. R. Meteorol. Soc.* **137**, 553–597 (2011).
65. Swales, D. J., Pincus, R. & Bodas-Salcedo, A. The cloud feedback model intercomparison project observational simulator package: Version 2. *Geosci. Model Dev.* **11**, https://doi.org/10.5194/gmd-11-77-2018 (2018).
66. Gjermundsen, A. et al. Shutdown of southern ocean convection controls long-term greenhouse gas-induced warming. *Nat. Geosci.* **14**, 724–731 (2021).
67. Zelinka, M. D., Klein, S. A., Qin, Y. & Myers, T. A. Evaluating climate models' cloud feedbacks against expert judgment. *J. Geophys. Res.* **127**, e2021JD035198 (2022).
68. Rugenstein, M. et al. Equilibrium climate sensitivity estimated by equilibrating climate models. *Geophys. Res. Lett.* **47**, e2019GL083898 (2020).
69. Bruno, O. Distributions of supercooled liquid fraction from caliop v4 https://zenodo.org/doi/10.5281/zenodo.8289057 (2022).

Acknowledgements

Author contributions

Competing interests

The authors declare no competing interests.

Additional information

Supplementary information The online version contains supplementary material available at https://doi.org/10.1038/s43247-024-01524-2.

Correspondence and requests for materials should be addressed to Stefan Hofer.

Peer review information *Communications Earth & Environment* thanks Kyle E. Fitch and Tim Myers for their contribution to the peer review of this work. Primary Handling Editors: Kyung-Sook Yun, Heike Langenberg. A peer review file is available.

Reprints and permissions information is available at http://www.nature.com/reprints

Publisher's note Springer Nature remains neutral with regard to jurisdictional claims in published maps and institutional affiliations.